Emergence of metachronal waves in active microtubule arrays

Stephen E. Martin,[1] Matthew E. Brunner,[2] and Joshua M. Deutsch [1,*]

[1]*Department of Physics, University of California, Santa Cruz, California 95064, USA*
[2]*Voltaiq Inc. 2150 Shattuck Ave, #704 Berkeley, California 94704, USA*

The physical mechanism behind the spontaneous formation of metachronal waves in microtubule arrays in a low-Reynolds-number fluid has been of interest for the past several years, yet is still not well understood. We present a model implementing the hydrodynamic coupling hypothesis from first principles and use this model to simulate kinesin-driven microtubule arrays and observe their emergent behavior. The results of simulations are compared with known experimental observations by Sanchez *et al.* [Science **333**, 456 (2011)]. By varying parameters, we determine regimes in which the metachronal wave phenomenon emerges and categorize other types of possible microtubule motion outside these regimes.

I. INTRODUCTION

Metachronal waves refer to the synchronization of thin, flexible appendages that result in large-scale wavelike formations. These appear in biological systems at the macroscopic scale (e.g., the motion of millipede legs) and at the microscopic scale (e.g., cilia in air pathways). On the microscopic level, metachronal waves are essential components of several critical biological processes, from motility in microorganisms to mucus clearance in human bronchial tubes [1,2]. If cilia are unable to effectively move and synchronize, the results are often severe—especially if the disorder is genetic [1]. Research into physical explanations for cilia beating [3], and of spontaneous metachronal behavior in cilia is ongoing and still not well understood [4,5], although many have suggested that this phenomenon can be explained from hydrodynamic coupling between cilia [6–9].

Recently, in some remarkable experiments, Sanchez *et al.* demonstrated metachronal wave behavior in an *in vitro* system [10,11]. Microtubules (MTs) aggregated into bundles of length 10–100 μm due to the addition of polyethylene glycol [12]. Many of these bundles are attached at one end to a fixed boundary forming dense arrays. When exposed to a solution containing clusters of kinesin and ATP, sustained metachronal wave behavior between MT bundles (similar to that displayed by cilia and flagella) was observed. MT bundles were constrained to move between two glass slides. It is surprising that a system with so few ingredients could develop complex behavior that so closely resembles biological systems, which are made up from a much more complicated machinery. Proteomic analysis indicates that eukaryotic cilia are composed of many hundreds of proteins [13].

Some important details of this *in vitro* system are still unclear, most notably whether the MTs in this experiment are unipolar or of mixed polarity. Opposite-polarity MTs will move past each other, causing separation into unipolar bundles [14,15]. We present analytical and numerical arguments for unipolarity in Appendix E. The surprising mechanism for the motion of unipolar bundles is
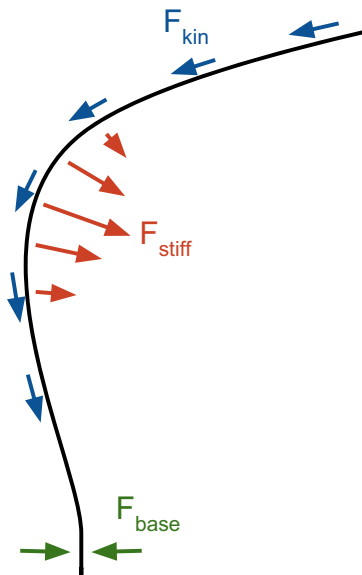
---

*josh@ucsc.edu

103101-1

FIG. 1. Conceptual illustration of forces acting on a single polymer that are not due to hydrodynamic interactions. The blue vectors indicate the buckling forces due to kinesin walkers (tangent to polymer), the red vectors show the direction and relative magnitude of stiffness forces (in the direction of $d^4\mathbf{r}/ds^4$), and the green arrows indicate a restorative force keeping the base of the polymer approximately perpendicular to the binding surface.

described here, and we believe that the agreement between our model and experiments provides further evidence to support our proposed explanation.

The general mechanism proposed is quite similar to the model used to describe and simulate cytoplasmic streaming in *Drosophila* oocytes, and the fact that it can be adapted as such is in many ways a testament to its predictive power. A fair amount of attention has been paid in recent years to the understanding of how metachronal waves form in such arrays [16–19]. However, such models often rely on assumptions about individual MT (or cilia) beat patterns and/or on phenomenology. The model we propose makes no such assumptions (beyond some minor simplifications), relying on first-principles fluid mechanics calculations. This is important because it is not clear why one would want additionally to impose oscillatory behavior on individual MTs given the lack of a well-defined internal structure.

II. THE MODEL

We now present a model for the simulation of the system of Sanchez *et al.* A similar method has been used successfully to simulate cytoplasmic streaming [20] in *Drosophila* oocytes [21] and is based on theoretical work completed several decades ago regarding the calculation of Stokes flows created by a point force (stokeslet) near no-slip boundaries [22,23]. A conceptual explanation of this mechanism is given below, and further details regarding theory and implementation are given in Appendixes B and C.

An illustration of how MT bundles are simulated is given in Fig. 1. Each MT bundle is modeled as a chain of monomers (i.e., polymer) which are held at an approximately fixed distance from one another by a spring force. The base of each polymer is anchored to a single point, and the polymer at the base is kept roughly perpendicular to the anchoring surface. Let the polymer be described by the curve $\mathbf{r}(s)$, where $\mathbf{r}(0)$ is the location of the polymer base, and s is the arc length. We give the

polymer a stiffness by implementing an energetic cost of bending proportional to curvature squared, which implies a local force at s proportional to $d^4\mathbf{r}/ds^4$. Additionally, monomers feel a "buckling" force due to the drag from the walking kinesin $F_{\text{kin}} = -f_k d\mathbf{r}/ds$, which is parallel to the polymer and toward the polymer base. f_k will depend linearly on the speed of the kinesin and the solvent viscosity. This force continually adds energy to the system (making it active) and has been shown to be a good representation of the average drag force due to kinesin walking along the microtubule away from the polymer base [21].

This kind of model for a single chain was first employed to understand glide assay dynamics in two dimensions [24]. In three dimensions, periodic waves develop whose dynamics have been analyzed in detail [21], and related theoretical work has recently also been performed [25]. However, scaling can be used to get the relevant length and timescales [24], and this survives when considering the full hydrodynamic treatment [21]. The average radius of curvature depends on the strength of the buckling force f_k and the elastic constant of a filament characterizing its stiffness k_{stiff}. The radius of curvature over quite a wide range of parameters can be shown to be $R = [k_{\text{stiff}}/(\beta f_k)]^{1/3}$, where $\beta \approx 0.05$. Likewise, the angular frequency is $\omega = f_k/(\nu R)$, where ν is the hydrodynamic drag coefficient per unit length. Although there is a fairly large experimental uncertainty in parameters used to model a *Drosophila* oocyte, this model finds quite good agreement with the experimental time and length scales. R was predicted to be 25–54 μm, close to the 16.3 ± 2.2 μm observed. Likewise, the timescale was predicted to be 203–1094 s, which is in the observed range of 370 ± 42 s. It is interesting that the length and timescales observed by Sanchez *et al.* are also quite close to these numbers, and that the frequency of biological cilia beating is often three orders of magnitude higher than this. See Appendix F for a detailed comparison with this experiment.

Polymers also feel hydrodynamic forces. As the force from the kinesin causes the polymers to buckle, we begin to see complex motion. Each monomer acts as a point force (stokeslet) in the surrounding fluid. This force that a monomer exerts on the fluid is simply the sum of all of the other forces on the monomer: because the Reynolds number is nearly zero, there are no inertial terms, meaning the force is transferred perfectly from the monomer to the fluid. Because this is a Stokes flow, the flow contributions from all stokeslets add linearly, and we can (in principle) calculate the flow everywhere. However, we only need to calculate the fluid velocity at points with monomers. Therefore, the evolution can be calculated via a pairwise sum over all monomers (see Appendix B).

It should be emphasized that, when motors walk up microtubules, the force produced by the motor is only one of many forces acting on the fluid. Newton's third law implies that the motor will apply the opposite force to the microtubule which will also act on the fluid. This leads to a cancellation of the long-range hydrodynamic component and the only remaining forces are from the microtubule's backbone; that is, curvature and tension forces, and it is these that create long-range flow. The simulation method that we employ (see the supplementary material of Ref. [21]) analyzes these forces quantitatively to derive the equations of motion for the system.

We also assume all polymer motion is two dimensional with a constant value of z, which is physically sensible when considering the geometry of the experiments of Sanchez *et al.* In this experiment, MT bundles were observed between glass slides, with a height H of approximately 10 μm creating a narrow channel through which fluid can flow. For this reason, we adopt a two-dimensional geometry. In addition, the no-slip boundaries of the plates have a large impact on the hydrodynamic forces between monomers [22,23], which we give explicitly in Appendix B. Other close-range contact forces were also used: monomer-monomer repulsion, which is small and allows chain crossing, and repulsion from the anchoring surface. See Appendix C.

We can now address, at the qualitative level, the proposed mechanism of formation for the metachronal waves observed by Sanchez *et al.* As kinesin walk away from the polymer bases, the polymers will tend to buckle. If a polymer is isolated, this buckling will lead to corkscrew motion or periodic waves [21]. When placed in an array, however, nearby polymers will exert hydrodynamic forces on one another that tend to synchronize their motion. If these hydrodynamic forces are sufficiently strong, this can cause a transition from disordered motion to aligned MTs and correlated motion.
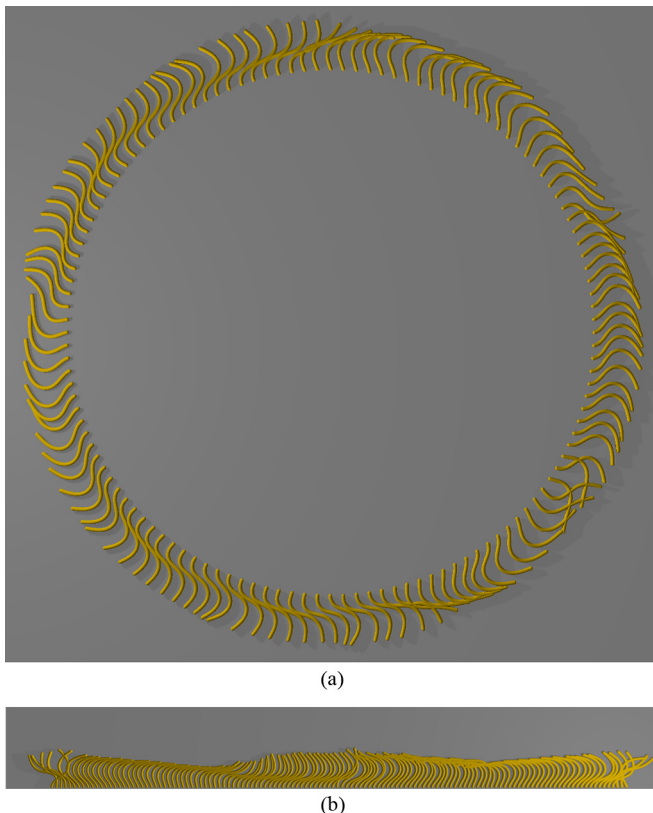
(a)

(b)

FIG. 2. Simulated metachronal wave formation for 128-polymer arrays in (a) circular and (b) planar geometries. In both cases, $k_{\mathrm{oseen}} = 0.1$, $k_{\mathrm{stiff}} = 10.0$, $H = 1$.

III. RESULTS

Despite the fact that this model was developed to explain and simulate cytoplasmic streaming, its mechanism can be easily adapted for related biological phenomena. Indeed, when the conditions of the experiment of Sanchez *et al.* are simulated in the same way, we observe metachronal waves. It is not clear if this is formally a transition or a more continuous crossover effect, but the results found make strong predictions that should be testable experimentally. In the following, we present the results of these simulations and discuss the required conditions for metachronal wave formation. Videos of select simulations are included in the Supplemental Material [26]. Figure 2 shows some still frames of simulated arrays demonstrating metachronal wave behavior in both the planar and circular geometries.

We characterize the behavior of each system using the correlation function for the chain ends $x(i, t)$,

$$C(\Delta i, \Delta t) = \langle \Delta x(i + \Delta i, t + \Delta t) \Delta x(i, t) \rangle, \tag{1}$$

where

$$\Delta x(i, t) = x(i, t) - \langle x(i, t) \rangle.$$

The average is performed over all chain indices i and time t, after a period of equilibration. Figures 3 and 4 show correlation functions for circular and planar geometries (for the circular geometry, the polar angle θ is the position variable rather than x). In the following, we discuss these and examine
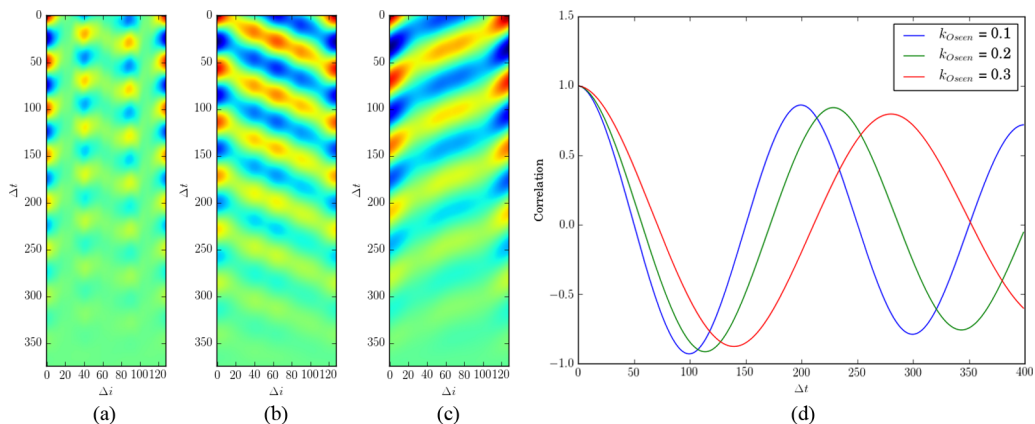
FIG. 3. Full correlation functions for circular geometry with $H = 1$ and $k_{\text{stiff}} = 10$, with $k_{\text{oseen}} = 0.1$, 0.2, and 0.3 in panels (a)–(c), respectively. The correlation function at $\Delta i = 0$ for all of these values of k_{oseen} are shown in panel (d).

how the system responds to changes in the strength of the interaction tensor, k_{oseen}, k_{stiff}, and height H. It should be noted that changes in the viscosity or kinesin velocity and density (that affect f_k), can be absorbed into a rescaling of time, and of k_{stiff}.

k_{oseen} has a dramatic effect on the type of wave behavior seen, or whether it is observed at all. This strength is a function of the hydrodynamic effects of kinesin walking along microtubules and will depend on their density and speed, as explained in detail in Ref. [21]. Figure 3 shows the correlation results of three 128-polymer simulations (monomer number = 16) in the same circular geometry shown in Fig. 2(a) for three different values of k_{oseen}. There is an overall strengthening of the metachronal behavior as k_{oseen} is increased from 0.1 to 0.2. The sign of the slope reflects the initial conditions of the system. Long-lived waves travel predominantly in a single direction over long times scales, resulting in a slope of the crests of the correlation function that can either be positive or negative. Similar crests are seen in the analysis of the real experimental data [10]. With this circular geometry, the correlation function must be periodic, which is why it rises again when i becomes large.
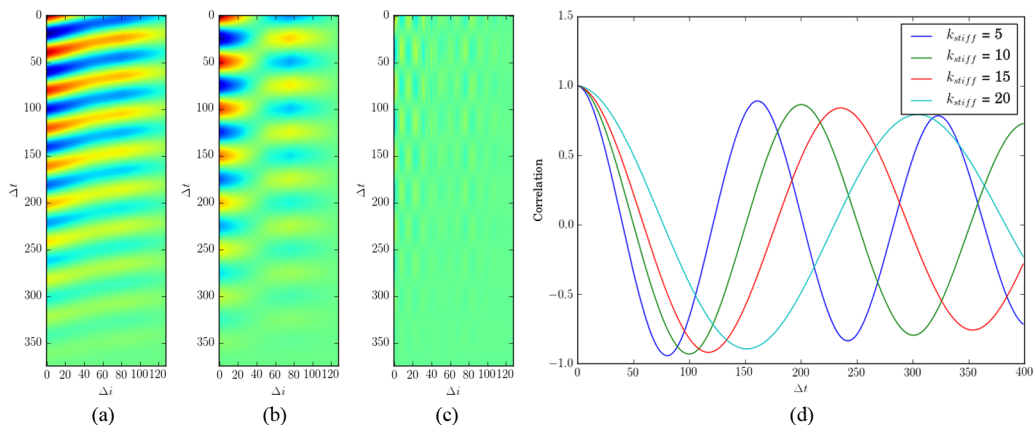

FIG. 4. Full correlation functions for planar geometry with $H = 1$ and $k_{\text{oseen}} = 0.1$, with $k_{\text{stiff}} = 5.0$, 10.0, and 20.0 in panels (a)–(c), respectively. The correlation function at $\Delta i = 0$ for all of these values of k_{stiff} are shown in panel (d).

The polymer stiffness k_{stiff} also has an interesting effect on metachronal wave formation. Figure 4 shows the correlation functions for $k_{stiff} = 5.0$, 10.0, and 20.0 in a planar geometry. While Figs. 4(a) and 4(b) both are indicative of an underlying system showing strongly periodic wavelike motion but with a spatial correlation length that is substantially shorter in 4(b) than in 4(a). Figures 4(c) and 4(d) show that, if the polymer is made too stiff, no metachronal behavior is observed at all. In general, planar geometry appears to cause more coherence in the motion of the different bundles, and the correlation function is dominated by motion at the longest lengths and timescales.

The distance between plates, H, has a considerable effect on the dynamics as well. Longer-range, more coherent motion is observed when H is larger, and short-range, less coherent motion when H is small (see Fig. 8 in the Appendix and supplementary videos S2 through S5 for more detailed information [26].) This is to be expected because of the strong screening effect that these boundary conditions impose. Smaller H reduces the hydrodynamic coupling, causing a decrease in coherence.

When comparing these results to those of Sanchez *et al.*, we find that the basic features agree. The videos included in the Supplemental Materials [26] qualitatively mimic the experimental videos (see Ref. [10] supporting materials), and the experimental correlation analysis of Sanchez *et al.* agrees quite well with the simulations. More importantly, this agreement between theory and experiment was reached from first principles. We only use a handful of forces in our simulations, and each force has a physical justification for being used.

IV. DISCUSSION

There are potential shortcomings of this model that may result in some differences between experiment and theory. The first is that the experiments observe bundles of microtubules that taper away from their base. The hydrodynamics are not expected to be uniform along the length of a chain. In addition, these bundles will, for short enough times, behave like rigid material, but for longer times, because they are connected through walking kinesin molecules, they will behave more as individual microtubules with a greatly reduced elastic constant. On the timescales of the motion, we expect to be in the latter regime. However, the details of the hydrodynamics and elasticity in these bundles is still not understood experimentally. In fact, as we mentioned earlier, the polarity of individual MT's is not known experimentally, and arguments for their unipolarity are given in Appendix E. But still, the basic mechanism of dynamic buckling due to kinesin drag and metachronal waves being generated by hydrodynamic coupling is robust over a wide parameter range, so we believe that these complications, aside from unipolarity, will not alter the basics of our explanation.

At a more technical level, there are other things that may make a slight difference to the results here. The bundles are constrained to move only in the xy plane, and while it is true that MT motion is nearly two-dimensional, there is some room in the z direction that MT bundles can occupy. Additionally, this model does not account for the fluid boundary condition at the anchoring surface. This may introduce some errors if a monomer becomes close ($\sim H$) to the anchoring plane. However, because of the screening effects of the plates, this should not alter the behavior at distances large compared with the plate separation. We have tested for this by adding image charges to the planar case, and found that their effects on correlations are small, as expected.

V. CONCLUSIONS

In conclusion, we have developed a model for the spontaneous formation of wavelike behavior in active polymer arrays that only requires two ingredients: semiflexible chains tethered to a surface, and motors walking from their bases to their tips. The hydrodynamics in their confined geometry gives rise to metachronal waves that appear remarkably similar to what is observed experimentally [10,11]. Unlike axonemes in cilia, there is no need to posit additional mechanisms that force individual bundles to oscillate. This all happens as a consequence of Newton's laws and fluid mechanics, allowing us to gain a better understanding of how metachronal waves form

with considerable predictive power. As such, we have examined new parameter spaces and have demonstrated boundaries between different types of metachronal behavior and regimes in which no metachronal behavior exists. It would be of great interest to test these predictions experimentally and, in many cases, this appears to be viable. Given the simplicity and robust nature of this mechanism, and the ubiquity of microtubules and kinesin in cells, it gives one further impetus to look for other places in biology where this kind of behavior can be found.

APPENDIX A: SUPPLEMENTARY VIDEO LEGENDS

Descriptions of the supplemental videos [26]:

Supplementary video S1. 128 microtubule bundles (length 16) with kinesin walkers in a circular geometry in a fluid chamber with $k_{\text{oseen}} = 0.1$, chamber height $H = 1.0$, $k_{\text{stiff}} = 10$.

Supplementary video S2. 128 microtubule bundles (length 16) with kinesin walkers in a circular geometry in a fluid chamber with $k_{\text{oseen}} = 0.2$, chamber height $H = 0.1$, $k_{\text{stiff}} = 10$.

Supplementary video S3. 128 microtubule bundles (length 16) with kinesin walkers in a circular geometry in a fluid chamber with $k_{\text{oseen}} = 0.2$, chamber height $H = 0.2$, $k_{\text{stiff}} = 10$.

Supplementary video S4. 128 microtubule bundles (length 16) with kinesin walkers in a circular geometry in a fluid chamber with $k_{\text{oseen}} = 0.2$, chamber height $H = 0.5$, $k_{\text{stiff}} = 10$.

Supplementary video S5. 128 microtubule bundles (length 16) with kinesin walkers in a circular geometry in a fluid chamber with $k_{\text{oseen}} = 0.2$, chamber height $H = 1.0$, $k_{\text{stiff}} = 10$.

Supplementary video S6. 128 microtubule bundles (length 16) with kinesin walkers in a circular geometry in a fluid chamber with $k_{\text{oseen}} = 0.3$, chamber height $H = 1.0$, $k_{\text{stiff}} = 10$.

Supplementary video S7. 128 microtubule bundles (length 16) with kinesin walkers in a planar geometry in a fluid chamber with $k_{\text{oseen}} = 0.1$, chamber height $H = 1.0$, $k_{\text{stiff}} = 5$.

Supplementary video S8. 128 microtubule bundles (length 16) with kinesin walkers in a planar geometry in a fluid chamber with $k_{\text{oseen}} = 0.1$, chamber height $H = 1.0$, $k_{\text{stiff}} = 10$.

Supplementary video S9. 128 microtubule bundles (length 16) with kinesin walkers in a planar geometry in a fluid chamber with $k_{\text{oseen}} = 0.1$, chamber height $H = 1.0$, $k_{\text{stiff}} = 15$.

Supplementary video S10. 128 microtubule bundles (length 16) with kinesin walkers in a planar geometry in a fluid chamber with $k_{\text{oseen}} = 0.1$, chamber height $H = 1.0$, $k_{\text{stiff}} = 20$.

Supplementary video S11. 2 microtubules of opposite polarities, green MT's have minus ends on surface, and blue MT's have plus ends on the surface. There are fixed boundary conditions on the surface. This shows a simulation for a set of parameters where the two microtubules move. This behavior was never found when there were more than 2 microtubules in a bundle.

Supplementary video S12. Pillar of nine microtubules of opposite polarities, green MT's have minus ends on surface, and blue MT's have plus ends on the surface. There are sliding boundary conditions on the surface. This shows a simulation in a regime with sufficiently weak attractive interactions, $f_a = 1$, where there is a twisting motion inside the pillar but then the minus microtubules suddenly slide off of the plus ones, finally lying close to parallel with the plane of attachment.

APPENDIX B: THE QUASI-TWO-DIMENSIONAL INTERACTION TENSOR

The interaction tensor used in simulations is that of a stokeslet enclosed by two infinite parallel plates, as derived by Liron and Mochon [23]. In general, the interaction tensor $\mathbb{G}$ is defined as the
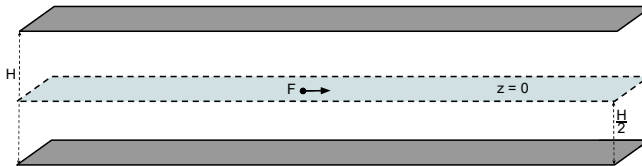
FIG. 5. Illustration of the geometry for which interaction tensor is derived in Appendix B. While this is a three-dimensional system, we constrain polymers to the xy plane.

relationship between the fluid flow $\mathbf{u}(\mathbf{r})$ and the stokeslet $\mathbf{F}$ which causes this flow:

$$\mathbf{u}(\mathbf{r}) = \mathbf{F} \cdot \mathbb{G}(\mathbf{r}). \tag{B1}$$

We assume that the system is embedded in a viscous fluid with viscosity μ. For computational efficiency, we assume all monomers to be only in the xy plane, with parallel plates at $z = \pm H/2$. This reduces a three-dimensional problem to two dimensions, as (a) the stokeslet is located in the xy plane, (b) the stokeslet's direction has no z component, and (c) we only concern ourselves with flows in the xy plane (see Fig. 5). For this arrangement, it can be shown from Liron and Mochon's general result that the interaction tensor a displacement $\mathbf{r}$ (and $\rho \equiv |\mathbf{r}|$) from a single stokeslet $\mathbf{F}$ at the origin reduces to

$$\mathbb{G}(\mathbf{r}) = \frac{H}{8\pi\mu\rho^2} \left\{ \left[4\left(\frac{\rho}{H}\right)^2 S_1 - \frac{1}{2}\frac{\rho}{H}I_1 \right] \mathbb{I} + \left[4\pi\left(\frac{\rho}{H}\right)^3 S_2 + \frac{1}{2}\frac{\rho}{H}I_1 - \frac{1}{4}\left(\frac{\rho}{H}\right)^2 I_2 \right] \frac{\mathbf{r}\otimes\mathbf{r}}{\rho^2} \right\}, \tag{B2}$$

where

$$S_1 \equiv \frac{1}{4}\sum_{n=0}^{\infty} \frac{(-1)^n}{\left[\left(\frac{\rho}{H}\right)^2 + n^2\right]^{1/2}}, \quad S_2 \equiv \frac{1}{4\pi}\frac{\rho}{H}\sum_{n=0}^{\infty} \frac{(-1)^n}{\left[\left(\frac{\rho}{H}\right)^2 + n^2\right]^{3/2}},$$

$$I_1 \equiv \int_0^{\infty} \xi J_1\left(\frac{\rho}{H}\xi\right)\frac{\tanh^2\frac{\xi}{2}}{\sinh\xi - \xi}d\xi, \quad I_2 \equiv \int_0^{\infty} \xi^2\left[J_0\left(\frac{\rho}{H}\xi\right) - J_2\left(\frac{\rho}{H}\xi\right)\right]\frac{\tanh^2\frac{\xi}{2}}{\sinh\xi - \xi}d\xi.$$

Here, J_n is the Bessel function of the first kind. Because S_1 and S_2 do not converge rapidly as defined above, we also make use of the Poisson sums

$$S_1 = \sum_{k=0}^{\infty} K_0\left[\pi(2k+1)\frac{\rho}{H}\right], \quad S_2 = \sum_{k=0}^{\infty}(2k+1)K_1\left[\pi(2k+1)\frac{\rho}{H}\right],$$

where K_n is the modified Bessel function of the second kind.

In the far field, it can be shown that (B2) approaches

$$\mathbb{G}(\mathbf{r}) \approx -\frac{3H}{32\pi\mu\rho^2}\left(\mathbb{I} - 2\frac{\mathbf{r}\otimes\mathbf{r}}{\rho^2}\right). \tag{B3}$$

Figure 6 shows plots of $\mathbf{u}(\mathbf{r})$ at selected locations and compares the exact value from Eq. (B2) to the far-field approximation from Eq. (B3).

We can now make some conceptual observations regarding this interaction tensor and how it compares to the boundary-free Oseen tensor $\mathbb{G}_0$:

$$\mathbb{G}_0(\mathbf{r}) = \frac{1}{8\pi\mu r}\left(\mathbb{I} + \frac{\mathbf{r}\otimes\mathbf{r}}{r^2}\right).$$

First, we immediately notice a $1/r$ dependence (rather than $1/\rho^2$). This means forces without boundaries tend to be more long range, and boundaries result in long-range screening. Second, $\mathbb{G}_0$ is always positive, whereas this is not true for the interaction tensor used here. One key implication of this is that flows created by a stokeslet are often flowing opposite its direction [e.g., Fig. 6(b)].
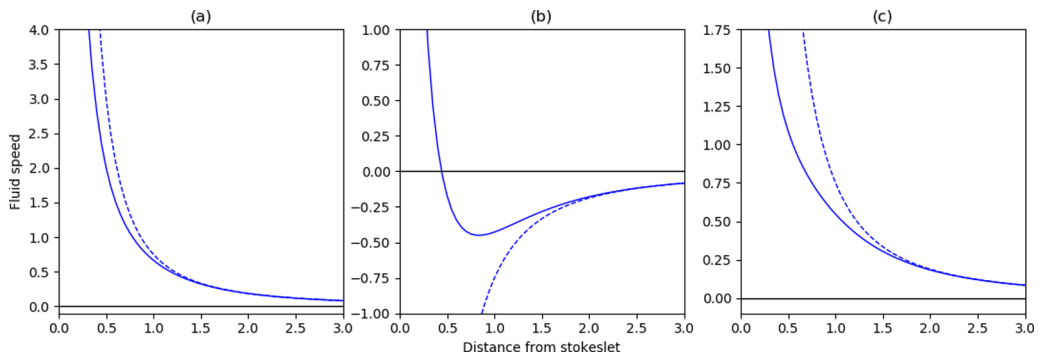
FIG. 6. Fluid speeds as a function of distance ρ from the stokeslet $\mathbf{F} = \hat{\imath}$. Solid curves are calculated by using the full interaction tensor (B2) and dashed lines are the far-field approximation (B3). (a) $u_x(\rho)$ along the line $y = 0$; (b) $u_x(\rho)$ along the line $x = 0$; (c) $u_y(\rho)$ along the line $y = x$.

Both of these qualities may enhance metachronal behavior in the confined system. Screening means that interactions between nearby polymers are most important, creating a "domino effect" from one polymer to the next rather than having motion more influenced by long-range interactions. The creation of opposing flows means (among other things) that if one polymer is moving toward the anchoring surface, it may exert a force on many of its neighboring polymers *away* from the anchoring surface. This encourages wavelike behavior rather than uniformity of beating motion.

APPENDIX C: SIMULATION METHODS

The algorithm we implement is built on work that was used to simulate the mechanism behind cytoplasmic streaming in *Drosophila* oocytes [21], and many of the methods and equations below are explained in detail in these papers. This software simulates an array of active microtubules tethered to a plane that works as follows and is explained in further detail below:

(1) After an array of polymers is initialized, forces on all monomers are summed (described below, also see Fig. 1 of main paper) and monomer position and velocity are updated using time step dt.

(2) This motion initiates complex flow in the surrounding fluid. The fluid flow is not simulated directly, but the resulting hydrodynamic forces from this flow are calculated via an Oseen tensor with corrections by Blake [22]. This is illustrated in Fig. 7.

(3) Forces on each monomer are summed, and monomer position and velocity are updated accordingly.

(4) Once updated, steps 2 and 3 are repeated.

In the present work there are the following differences:

(1) N Microtubules are confined to the xy plane, with polymer bases separated by a distance l tethered either to a flat plate at $y = 0$ or to a circular boundary. For all presented results, $N = 128$. The geometry of this is shown in Fig. 5.

(2) At the tethering point, a potential was added in order to keep the base monomer approximately orthogonal to the boundary.

(3) Rather than the Blake correction to the Oseen tensor, we use the simplified Liron-Mochon interaction tensor described in Appendix B. We also investigated varying the hydrodynamic coupling parameter $k_{\text{oseen}} \equiv 1/(8\pi\mu)$.

Now we describe how the above was accomplished in more detail. Each polymer is composed of $n = 16$ monomers. The ith monomer position $\mathbf{r}_i$ is updated a using a fourth order Runge Kutta
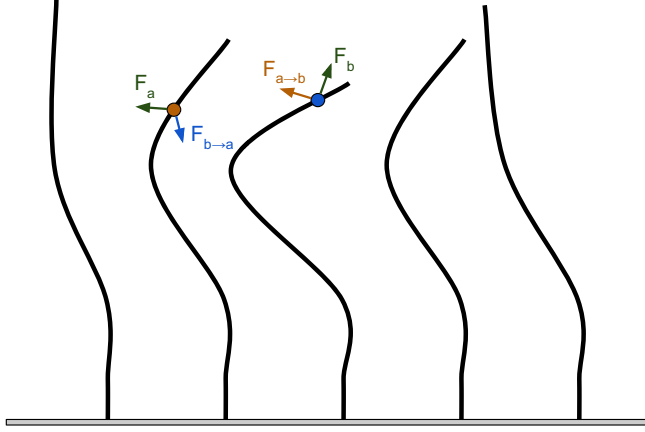
FIG. 7. Illustration of hydrodynamic forces between two example monomers in a planar polymer array. The green forces are the sum of nonhydrodynamic forces on the monomer (and by extension the force the monomer exerts on the surrounding fluid). $\vec{F}_{a \to b}$ and $\vec{F}_{b \to a}$ are the hydrodynamic forces on monomer b due to $\vec{F}_a$ and the hydrodynamic force on monomer a due to $\vec{F}_b$, respectively.

integration of the equation

$$\frac{d\mathbf{r}_i}{dt} = \mathbf{u}(\mathbf{r}_i) - k_{\text{kin}}(\mathbf{r}_{i-1} - \mathbf{r}_{i+1}), \tag{C1}$$

where dt is the time step (set to 0.003), k_{kin} (set to 0.2) controls the strength of the kinesin force tangent to the polymer ($\mathbf{F}_{\text{kin}}$ in Fig. 1), and $\mathbf{u}(\mathbf{r}_i)$ is the fluid velocity due to the motion of all other monomers as given by Eqs. (B1) and (B2) (which imparts the forces $\mathbf{F}_{a \to b}$ in Fig. 7):

$$\mathbf{u}(\mathbf{r}_i) = \sum_{j \neq i} \mathbf{F}_j \cdot \mathbb{G}(\mathbf{r}_i - \mathbf{r}_j). \tag{C2}$$

Here, $\mathbf{F}_j$ is the total force on the fluid due to the jth monomer. Because there are are no inertial effects when $\text{Re} \ll 1$, any nonhydrodynamic force exerted on the monomer must be transferred to the fluid. In our case,

$$\mathbf{F}_j = \mathbf{T}_j + \mathbf{C}_j + \mathbf{Q}_j, \tag{C3}$$

where

(i) $\mathbf{T}_j = k_{spr}[(|\mathbf{r}_{j-}| - \ell)\hat{\mathbf{r}}_{j-} + (|\mathbf{r}_{j+}| - \ell)\hat{\mathbf{r}}_{j+}]$, with $\mathbf{r}_{j\pm} \equiv \mathbf{r}_{j\pm1} - \mathbf{r}_j$, is the spring force keeping monomer separation approximately constant. For our simulations, $k_{spr} = 100$ and $\ell = 1$. In these simulations the separation between polymer bases defines above, l is equal to 4ℓ.

(ii) $\mathbf{C}_j = k_{\text{stiff}}(2\mathbf{r}_i - \mathbf{r}_{i+2} - \mathbf{r}_{i-2})$ is the stiffness force which resists polymer bending. k_{stiff} is varied in our simulations, but typically $5 \leqslant k_{\text{stiff}} \leqslant 20$.

(iii) $\mathbf{Q}_j = \mathbf{P}_j + \mathbf{B}_j + \mathbf{W}_j + \sum_k \mathbf{H}_{jk}$ is the sum of miscellaneous conditional forces:

(a) $\mathbf{P}_j = k_{\text{pin}}(\mathbf{r}_j - h\hat{\boldsymbol{j}})$ if $(j \mod n) = 1$ is the force on the base monomer of each polymer chain keeping it pinned to the anchoring surface. For our simulations, we set $k_{\text{pin}} = 100$ and $h = 1$.

(b) $\mathbf{B}_j = k_{\text{pin2}}(\mathbf{r}_j - \mathbf{r}_{j-1} - \ell\hat{\boldsymbol{j}})$ if $(j \mod n) = 2$ is the force on the second monomer in each polymer chain, keeping the base of each polymer approximately orthogonal to the anchoring surface (F_{base} in Fig. 1). For our simulations, we set $k_{\text{base}} = 100$.

(c) $\mathbf{W}_j = k_{\text{wall}}[1 - (\frac{d_{\text{wall}}}{y_j})^4]\hat{\boldsymbol{j}}$ if $y_j < d_{\text{wall}}$ is the repulsive force exerted by the anchoring plane on any monomer that gets close to the wall. For our simulations, we set $d_{\text{wall}} = 0.5$ and $k_{\text{wall}} = 100$.
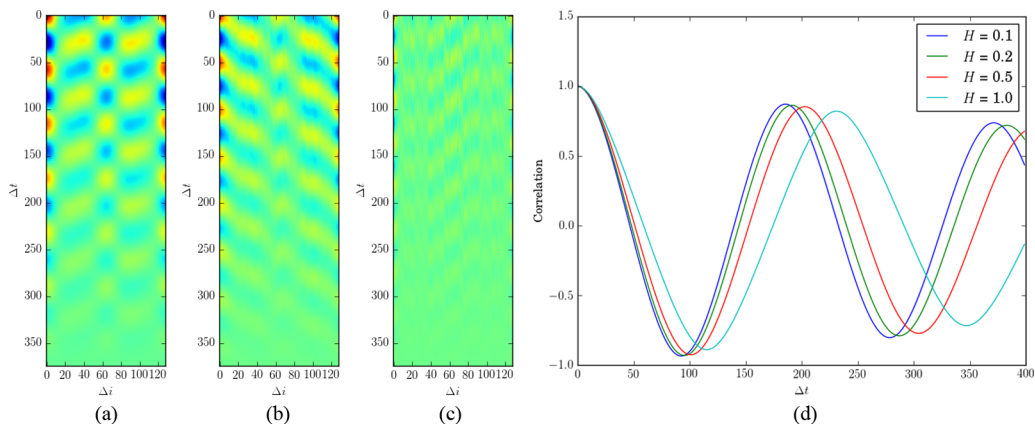
FIG. 8. Full correlation functions for circular geometry with $k_{\text{stiff}} = 10$, $k_{\text{oseen}} = 0.2$, and $H = 1.0$, 0.5, and 0.1 in panels (a) and (c), respectively. The correlation function at $\Delta i = 0$ for all of these values of H are shown in panel (d).

(d) $\mathbf{H}_{jk} = k_{\text{rep}}[1 - (\frac{d_{\text{rep}}}{|\mathbf{r}_j - \mathbf{r}_k|})^4](\mathbf{r}_j - \mathbf{r}_k)$ if $|\mathbf{r}_j - \mathbf{r}_k| < d_{\text{rep}}$ is the repulsive force between monomers that are very close to one another. For our simulations, we set $d_{\text{rep}} = 0.5$ and $k_{\text{rep}} = 1$.

APPENDIX D: CORRELATIONS VERSUS CHAMBER HEIGHT

In addition to varying chain stiffness, and the hydrodynamic coupling, and the geometry, we also varied the distance between the two plates, because this is also possible to probe experimentally. The results for the correlation functions are shown in Fig. 8, for 128 chains in a circular geometry, with $k_{\text{stiff}} = 10$, $k_{\text{oseen}} = 0.2$, and $H = 1.0$, 0.5, and 0.1. As is apparent from these figures, the motion becomes less correlated as H becomes smaller. In Fig. 8(a), there are strong correlations at different positions Δi, and from the slopes of the ridges and troughs, this shows the propagation of waves. Figures 8(b) and 8(c) show progressively less spatial correlation due to stronger screening by the plates. In Fig. 8(c), where $H = 0.1$, the motion is quite short range. This is also apparent from the supplementary videos S2 through S5.

APPENDIX E: ANALYSIS OF UNIPOLARITY

The work of Sanchez *et al.* [10,11] consists of a mixture of biotin-labeled kinesin-1 motors bound together to form clusters using multimeric streptavidin and taxol stabilized microtubules in a polyethylene-glycol solution with ATP. These form bundles of microtubules, some of which are adsorbed to air-water or air-glass interfaces, that point out from the interface forming a lawn of microtubule bundles. These bundles are flexible and show bending similar to what is seen in the simulations described here in both the timescales, length scales, and correlations between different bundles.

The question that is not answered in the experimental work is the directionality of the microtubules inside a bundle. The microtubules forced into bundles by the polyethylene glycol (PEG) could be of mixed polarity so that some have their minus ends at the interface while others have their plus ends there. We will refer to microtubules with different orientations as having different "polarities," minus-ends against the interface as "minus" and those with opposite polarity as "plus."

The problems with having a mixed polarity bundle are twofold: The first is that for a wide range of experimental parameters, we expect mixed polarity bundles to be unstable [14,15]. The second problem is that it is not clear that mixed polarity bundles can give rise to the motion seen experimentally. We will analyze both problems below.

1. Instability of mixed polarity bundles

The first problem is that adjacent microtubules with different polarities will be linked by kinesin clusters that will apply equal and opposite forces to them. This will cause the minus microtubules to be pushed toward the interface, and the plus ones away from it. The forces from the kinesin act in parallel on a microtubule over its length which is of order 10 μm. The forces that these cause can be competitive with depletion forces caused by the PEG, as we will now see. A full analysis of this is not possible without more information about the details of the system such as the density of kinesin clusters and chain lengths of the PEG. However we can do a calculation to show that even with very modest assumptions concerning kinesin density, expulsion of plus microtubules will take place.

Depletion forces exert an osmotic pressure on microtubules and filaments. Each polymer excludes a roughly spherical region on the order of its radius of gyration R_g. Entropic forces favor the separation of microtubules into bundles because less volume is excluded by the PEG. We estimate the force acting on a single microtubule protruding from a bundle. PEG is depleted in a region of size R_g around the microtubule. The increase in free energy per unit area caused by this depletion is of order pR_g where the osmotic pressure is $p = k_B T \rho$, and ρ is the number of polymers per unit volume. The increase in free energy dF, in raising the microtubule by a height dz, is $dF = (2\pi R_m dz)px$. Here R_m is the microtubule radius. If we assume that the polymers are close-packed around the microtubule to get the maximum effect, then $\rho = 1/(4\pi R_g^3/3)$. So the force needed to push the microtubule out of the tip of the bundle is $f = dF/dz = (3/2)R_m k_B T/R_g^2$.

$R_m \approx 13$ nm and conservatively taking $R_g = 1$ nm, which is quite small for PEG, $f = 81$ pN The stall force of kinesin is approximately 5 pN [27]. So only 16.2 kinesins are needed to overcome the depletion forces and expel this microtubule from the bundle.

The minimum separation of kinesin on a microtubule is 8 nm and there are 13 tracks around its circumference. Because kinesin has a strong affinity for microtubules we expect a high density of bound kinesin. Therefore 16 kinesins contributing to the force over a distance of 10 μm is over three orders of magnitude less dense than the maximum density attainable. This suggests that, for a wide range of parameters, the microtubule bundles will become unipolar with minus-ends against the interface.

2. Model of mixed polarity bundles

The second problem is that it is not clear that a mixed polarity bundle can give rise to the motion seen in experiment. Here we analyze this possibility by using simulation methods similar to what was used previously to understand molecular motor dynamics [28].

We assume that the microtubules are inextensible and that opposite polarity microtubules apply forces in equal and opposite directions. We discuss the different forces separately.

First there is an effective attractive interaction between microtubules independent of their polarities induced by the presence of PEG polymers. We choose a short-range force so the monomers separated by a distance $\mathbf{r}$ within a range σ_s will feel an attractive force due to depletion forces as discussed above. To simplify the expressions we use a normalized unitless distance $\Delta \equiv \mathbf{r}/\sigma_s$. The force between any two monomers for $\Delta < 1$ is taken to be

$$\mathbf{f}_{\text{attr}} = f_a \Delta^4 (1 - \Delta^{12})^3 \mathbf{r}, \tag{E1}$$

where f_a is the strength of the attractive interaction. The reason for choosing this functional dependence on Δ was to produce a force that was close to constant for $\Delta < 0.6$, and then drop smoothly to zero, so as to work well with the Runge Kutta algorithm.

Second, we introduce an even-shorter-range repulsion between monomers that diverges at a hard-core radius σ_h and goes to zero at σ_s:

$$\mathbf{f}_{\text{rep}} = f_r \left(\frac{1}{r^2 - \sigma_h^2} - \frac{1}{\sigma_s^2 - \sigma_h^2} \right)^4 \mathbf{r}, \tag{E2}$$

where f_r is the strength of the repulsive interaction.

Third, we introduce an equal and opposite forces between monomers on opposite polarity microtubules that are within a distance σ_s. The direction of the force is as follows: We compute the tangents to both monomers as $(\mathbf{r}_{i+1} - \mathbf{r}_{i-1})/2$. Then we choose the direction $\mathbf{t}$, to be the average of these two tangents. The magnitude of the kinesin force is

$$\mathbf{f}_{\text{kin}} = f_k(1 - \Delta^{12})^3, \tag{E3}$$

where f_k is similar the symbol used previously in the main text and denotes the magnitude of the kinesin force.

These forces are added to the elastic forces, viscous drag, and tension that must be introduced to conserve link length and the equation of motion is iterated by using a method for updating chains with constant link length [29,30].

We also tried two separate kinds of boundary conditions: first, tethering the chains to fixed points on the surface which we will call "fixed" boundary conditions; and second, confining the chain ends to a two-dimensional plane but letting the ends move within that plane, which we will call "sliding" boundary conditions.

We tried a wide range of parameters, of different elastic constants, attractive interactions, number of microtubules, and boundary conditions. What we found is now summarized.

For two chain bundles of opposite polarity we did find a set of parameters which showed movement of the bundle, with $f_r = 10.0$, $\sigma_s = 2$, $\sigma_h = 1$, $f_a = 3$, $f_k = 0.2$, $k_{\text{stiff}} = 100$, and a chain length of 20; see supplemental video S11.

For larger bundle sizes, e.g., nine chains, we did not find anything similar to experiments. With fixed boundary conditions, and starting as a pillar of parallel microtubules with slightly randomized directions, the chains would settle down to a pillar shape that would not change with time for sufficiently small attractive interactions f_a, but when this became greater than a certain value that depends on elastic constant and other parameters, it would suddenly collapse into a ball because this is more highly favored energetically.

When we chose sliding boundary conditions, and for sufficiently weak attractive interactions, $f_a = 1$ there was a regime where there was twisting motion inside the pillar but then the minus microtubules would suddenly slide off of the plus ones, finally lying close to parallel with the plane of attachment; see supplemental video S12. It therefore appears that a two-microtubule bundle moves because of a strong anisotropy in forces seen in cross sections. In larger bundles, the forces through the bundle are more homogeneous which acts to stabilize them.

We conclude that, by direct physical modeling of a mixed polarity bundle, it is not clear if there are any reasonable parameters which show motion similar to what is seen in the experiments of Sanchez *et al.* [10,11].

Note that the elastic constant of a microtubule in a bundle will depend strongly on the rate at which it is bent. For very short times, the bonds between different microtubules caused by kinesin binding will be fixed in position, giving the bundle the elastic constant of a cylinder of radius R which is $\propto R^4$. However, the oscillations here take place on minute timescales. In that case the individual kinesin molecules have velocities of order 1 μm/s so they unbind and move very far on this timescale. This allows neighboring microtubules to move relative to each other, to eliminate stress. Therefore on sufficiently long timescales, this reduces the elastic constant of a microtubule to that of one in isolation.

APPENDIX F: QUANTITATIVE COMPARISON WITH EXPERIMENT

We briefly summarize the protocol and procedures used to create the experimental system that we are trying to understand and compare those findings with our theory. This comparison is similar to what was done in the context of cytoplasmic streaming [21].

Microtubules were prepared by using methods to minimize intermicrotubule crosslinking. Their lengths were 4.8 ± 4.1 μm. Kinesin streptavidin complexes were created and added to the

microtubules along with polyethylene glycol (PEG). PEG introduces depletion forces discussed above in Appendix E 1 that will cause the microtubules to form bundles. The kinesin streptavidin complexes link individual kinesin motors together so that they walk up bundles together. Depending on the concentration of PEG, different dynamics and morphologies are seen. Concentrations between 0.5% to 0.6% are apparently optimal for observing beating bundles.

Many other chemical components were added to stabilize this system, particularly during photobleaching, but, crucially, ATP was added to make the kinesin motors active.

The resultant microtubule bundles were approximately 100 μm long and slowly tapered in diameter. Examination of images [10,11] shows that close to the air interface, bundles merge forming what appears to be a single bundle of diameter 1–2 μm that slowly tapers to become too thin to accurately measure, less than 0.1 μm. These bundles are made up of many small microtubules much smaller than the bundle length. No measurements of the bundle stiffness was attempted; however, translation of individual microtubules was observed by photolabeling. This is further evidence that the bundles were not strongly crosslinked and that the elastic properties are determined largely by the depletion forces that create the bundles in the first place. Microtubules can easily slide relative to each other, because streptavidin crosslinked motors do not walk in lock-step so that two motors walking up microtubules can relax any shear forces.

The time and length scales are quite similar to what was found previously in cytoplasmic streaming in *Drosophila* oocytes [21]. Although the bundle stiffness is unknown, our mechanism predicts a simple relationship between length and timescales for beating of an individual bundle.

We can model [21] an individual bundle as a thin elastic rod with a local drag coefficient per unit length ν and a force per unit length f_k caused by the drag of the kinesin motors walking up a bundle. The force on a rod oriented either perpendicular or parallel to the direction of motion only has a logarithmic dependence (for an infinite system) on its radius [31] and is linearly proportional to the length of the cylinder and the viscosity. With experimental conditions, a saturated surface containing kinesin walking at speed v_k will have $f_k \approx \nu v_k$. In the case of kinesin, $v_k \approx 0.8 \ \mu$m/s [32]. This was analyzed in detail in Ref. [21].

A tethered rod subject to these forces will show oscillatory motion that can be analyzed in mathematical detail [21]. Its angular frequency

$$\omega = f_k/(\nu R), \tag{F1}$$

where R is the radius of curvature. This equation is useful to consider here because it gives a relationship between radius of curvature and frequency that does not require a direct knowledge of chain stiffness. Furthermore, it does not require a knowledge of viscosity because f_k and ν are both proportional to it. This is an exact result for a single-chain analysis giving the relationship between the angular frequency ω, the force per unit length applied by the kinesin, the drag coefficient of the kinesin ν, and the radius of curvature R. It is exact when the rod is far from any surfaces, but has been analyzed both numerically and analytically for a single chain when there are velocity fields and surfaces present. For a large range of parameters, this relation is close to being exact. However, this analysis ignores long-range hydrodynamic interactions, but simulations [21] including such effects agree quite well with this model. From Eq. (F1) we see that $\omega = 2\pi f = \nu v_k/(\nu R) = v_k/R$. From experimental images [10,11], the radius of curvature R is approximately 30 μm. Therefore the frequency of oscillation is predicted to be 4.1×10^{-3} Hz. The experimentally measured number from Ref. [1], is 4.8×10^{-3} Hz. Given large experimental uncertainties, this result is fortuitously close, and we would expect more generally that it should agree within a factor of two.

We can also estimate the force on a single kinesin motor and compare it with the stall force. For a cylinder moving in solution with a viscosity η, approximately that of water, and ignoring logarithmic corrections, the force per unit length will be $f_k = \eta v_k \sim 8 \times 10^{-10}$N/m. In our model kinesin motors, close to saturation, walk on the surface of a bundle. The force on a single motor can be calculated by distributing f_k over all motors in a given length. Given a bundle of radius r_b, the number of motors per unit length is $N_k = 2\pi r_b/l_k^2$, where l_k is the size of a kinesin motor. Therefore the force on a single motor is $F = f_k/N_k$. In the extreme case where $l_k = r_b$, and estimating

$l_k = 10$ nm, this gives a force of $\sim 2.5 \times 10^{-18}$ N $= 2.5 \times 10^{-6}$ pN, where as the stall force is approximately 5 pN [33], this is more than a million times larger than what is needed for this model. More realistically, the radius of the bundle is much larger than this, by a factor of at least 100, making the force even smaller. Therefore, we can safely ignore the stall force or any velocity dependent effects, including those related to processivity.

---

[1] B. A. Afzelius, Cilia-related diseases, J. Pathol. **204**, 470 (2004).

[2] Y. Okada, S. Takeda, Y. Tanaka, J.-C. I. Belmonte, and N. Hirokawa, Mechanism of nodal flow: A conserved symmetry breaking event in left-right axis determination, Cell (Cambridge, MA, U. S.) **121**, 633 (2005).

[3] C. J. Brokaw, Molecular mechanism for oscillation in flagella and muscle, Proc. Natl. Acad. Sci. USA **72**, 3102 (1975).

[4] S. Camalet, F. Jülicher, and J. Prost, Self-Organized Beating and Swimming of Internally Driven Filaments, Phys. Rev. Lett. **82**, 1590 (1999).

[5] C. B. Lindemann and K. A. Lesich, Flagellar and ciliary beating: The proven and the possible, J. Cell Sci. **123**, 519 (2010).

[6] M. A. Sleigh, Int. Rev. Cytol. **25**, 31 (1969).

[7] *Cilia and Flagella*, edited by M. A. Sleigh (Academic Press, London, New York, 1974).

[8] L. Gheber and Z. Priel, Biophys. J. **55**, 183 (1989).

[9] S. Gueron, K. Levit-Gurevich, N. Liron, and J. J. Blum, Cilia internal mechanism and metachronal coordination as the result of hydrodynamical coupling, Proc. Natl. Acad. Sci. USA **94**, 6001 (1997).

[10] T. Sanchez, D. Welch, D. Nicastro, and Z. Dogic, Cilia-like beating of active microtubule bundles, Science **333**, 456 (2011).

[11] T. Sanchez and Z. Dogic, Engineering oscillating microtubule bundles, in *Methods in Enzymology* (Elsevier, 2013), Vol. 524, pp. 205–224.

[12] D. J. Needleman, M. A. Ojeda-Lopez, U. Raviv, K. Ewert, J. B. Jones, H. P. Miller, L. Wilson, and C. R. Safinya, Synchrotron X-Ray Diffraction Study of Microtubules Buckling and Bundling Under Osmotic Stress: A Probe of Interprotofilament Interactions, Phys. Rev. Lett. **93**, 198104 (2004).

[13] G. J. Pazour, N. Agrin, J. Leszyk, and G. B. Witman, Proteomic analysis of a eukaryotic cilium, J. Cell Biol. **170**, 103 (2005).

[14] K. Kruse and F. Jülicher, Actively Contracting Bundles of Polar Filaments, Phys. Rev. Lett. **85**, 1778 (2000).

[15] T. B. Liverpool and M. C. Marchetti, Instabilities of Isotropic Solutions of Active Polar Filaments, Phys. Rev. Lett. **90**, 138102 (2003).

[16] M. C. Lagomarsino, P. Jona, and B. Bassetti, Metachronal waves for deterministic switching two-state oscillators with hydrodynamic interaction, Phys. Rev. E **68**, 021908 (2003).

[17] B. Guirao and J.-F. Joanny, Spontaneous creation of macroscopic flow and metachronal waves in an array of cilia, Biophys. J. **92**, 1900 (2007).

[18] J. Elgeti and G. Gompper, Emergence of metachronal waves in cilia arrays, Proc. Natl. Acad. Sci. USA **110**, 4470 (2013).

[19] T. Niedermayer, B. Eckhardt, and P. Lenz, Synchronization, phase locking, and metachronal wave formation in ciliary chains, Chaos **18**, 037128 (2008).

[20] L. R. Serbus, B.-J. Cha, W. E. Theurkauf, and W. M. Saxton, Dynein and the actin cytoskeleton control kinesin-driven cytoplasmic streaming in drosophila oocytes, Development **132**, 3743 (2005).

[21] C. E. Monteith, M. E. Brunner, I. Djagaeva, A. M. Bielecki, J. M. Deutsch, and W. M. Saxton, A mechanism for cytoplasmic streaming: Kinesin-driven alignment of microtubules and fast fluid flows, Biophys. J. **110**, 2053 (2016).

[22] J. R. Blake, A note on the image system for a stokeslet in a no-slip boundary, Math. Proc. Cambridge Philos. Soc. **70**, 303 (1971).

[23] N. Liron and S. Mochon, Stokes flow for a stokeslet between two parallel flat plates, J. Eng. Math. **10**, 287 (1976).

[24] L. Bourdieu, T. Duke, M. B. Elowitz, D. A. Winkelmann, S. Leibler, and A. Libchaber, Spiral Defects in Motility Assays: A Measure of Motor Protein Force, Phys. Rev. Lett. **75**, 176 (1995).

[25] G. De Canio, E. Lauga, and R. E. Goldstein, Spontaneous oscillations of elastic filaments induced by molecular motors, J. R. Soc., Interface **14**, 20170491 (2017).

[26] See Supplemental Material at http://link.aps.org/supplemental/10.1103/PhysRevFluids.4.103101 for videos of the simulations.

[27] E. Meyhöfer and J. Howard, The force generated by a single kinesin molecule against an elastic load, Proc. Natl. Acad. Sci. USA **92**, 574 (1995).

[28] J. M. Deutsch and S. E. Martin, Photomechanical energy conversion using polymer brush dissociation, Macromolecules (Washington, DC, US) **48**, 6703 (2015).

[29] J. Deutsch, Theoretical studies of DNA during gel electrophoresis, Science **240**, 922 (1988).

[30] J. M. Deutsch and T. L. Madden, Theoretical studies of DNA during gel electrophoresis, J. Chem. Phys. **90**, 2476 (1989).

[31] H. Lamb, *Hydrodynamics* (Cambridge University Press, 1993).

[32] D. Cai, K. J. Verhey, and E. Meyhöfer, Tracking single kinesin molecules in the cytoplasm of mammalian cells, Biophys. J. **92**, 4137 (2007).

[33] K. Svoboda and S. M. Block, Force and velocity measured for single kinesin molecules, Cell (Cambridge, MA, US) **77**, 773 (1994).